RSC Mechanochemistry

ROYAL SOCIETY OF CHEMISTRY

REVIEW

View Article Online
View Journal | View Issue

Cite this: *RSC Mechanochem.*, 2025, **2**, 786

Mechanochemical conversion of elemental sulfur into functional sulfur nanomaterials for promising applications

Hammad Hasan, † Farwa Arshad † and Md Palashuddin Sk *

This review highlights the growing role of mechanochemistry in the synthesis and functionalization of sulfur-based nanomaterials. It begins with a conceptual and historical overview of mechanochemical processes, emphasizing how mechanical energy enables selective bond cleavage, defect formation, and structural transformations in solids. Particular focus is placed on the mechanochemical synthesis of sulfur nanomaterials, where mechanical activation overcomes the inherent chemical inertness of elemental sulfur, promoting the formation of nanodots and other nanostructures. Subsequent sections explore the structural, optical, and photophysical properties of these materials, including light absorption, photoluminescence (PL), optical stability, time-resolved photoluminescence (TRPL), and circularly polarized luminescence (CPL). These properties are strongly influenced by stress-induced defects and crystallinity, which are hallmark features of the mechanochemical approach. The review further surveys a range of application areas such as sensing, catalysis, and energy conversion, where sulfur nanomaterials exhibit promising performance owing to their unique physicochemical properties. In conclusion, we address current challenges, including defect control and the need for a deeper mechanistic understanding, and propose future directions for expanding the scope and enhancing the utility of mechanochemical methods in nanochemistry. Overall, this work underscores the potential of mechanochemistry not only as a green, solvent-free synthesis strategy but also as a powerful platform for uncovering novel functionalities in sulfur-based nanomaterials.

Received 18th April 2025
Accepted 28th August 2025

DOI: 10.1039/d5mr00051c

rsc.li/RSCMechanochem

1. Introduction

Sulfur, the 10th most abundant element in the universe and a key component of Earth's geochemical cycles, has played a pivotal role in advancing chemistry and materials science. Elemental sulfur, which is abundantly available as a low-cost byproduct of hydrodesulfurization processes in the petroleum and natural gas industries, presents both a challenge and an opportunity. With global sulfur production exceeding 70 million tons annually, the urgent need to valorize this surplus into functional, high-value products has emerged as a focal point of research in sustainable chemistry.[1–4] Traditionally, sulfur's utility has been confined to sectors such as agriculture (fertilizers), vulcanized rubber production, and industrial chemicals like sulfuric acid. However, its potential as a precursor for advanced materials remains underexplored. Sulfur's unique properties, such as its multiple oxidation states, high energy density, and diverse allotropes, make it a versatile candidate for applications ranging from nanotechnology to clean energy.[5–7] Recent breakthroughs have further demonstrated its potential in photonics, catalysis, energy storage, and environmental remediation, signalling a paradigm shift in how elemental sulfur is perceived within materials science.[8–11]

In this context, mechanochemistry has emerged as a game-changing methodology for the sustainable synthesis of sulfur-based materials. Mechanochemistry refers to the application of mechanical energy, *via* grinding, milling, or shearing, to drive chemical transformations in the solid state. Unlike conventional solution-phase methods, mechanochemical reactions eliminate or significantly reduce the use of solvents, making them environmentally benign and energy-efficient.[12] Table 1 summarizes the merits of mechanochemistry in contrast to other synthetic approaches.[13–18] Furthermore, the mechanochemical approach enables access to metastable phases, unusual bonding arrangements, and unique nanostructures that are often inaccessible through traditional synthetic techniques.[19] The versatility of mechanochemistry is particularly suited to sulfur, an element that often exhibits sluggish reactivity under standard conditions. Mechanochemical methods overcome these challenges by harnessing localized heat, pressure, and shear forces to break sulfur–sulfur bonds and facilitate reaction pathways.[20,21] These methods have enabled the direct conversion of elemental sulfur into a variety

Department of Chemistry, Aligarh Muslim University, Aligarh 202002, Uttar Pradesh, India. E-mail: palashuddin.ch@amu.ac.in

† Equal contribution.

Table 1 Comparative table for the merits and demerits of various synthetic approaches in contrast to mechanochemistry

Synthetic method	Merits	Demerits	References
Mechanochemistry	• High yield • Highly scalable and able to be carried out under flow conditions • Reaction rate is faster • Solvent free or minimal solvent usage	• Particle size is challenging to control • Need to purify the sample, due to the presence of impurity	13–15
Hydrothermal	• Better control over the size of particles • Pure crystalline phases	• Relatively lower yield and is subject to reactant concentration, temperature and pressure • Scaling up is challenging • Reaction rate is longer up to hours • Require high pressure and temperature	16
Solvothermal	• Precise control over particle size • Highly crystalline structure	• Yield is subject to reaction conditions • Scaling up is challenging • Reaction rate is slower • Requires high temperature and pressure	17
Vapor-phase	• Precise control over thin film deposition	• Yield is subject to rate of deposition • Complex reaction procedure • Scaling up is challenging	18

of functional nanostructures. These include sulfur nanoparticles (SNP), sulfur–carbon composites, and sulfur quantum dots (Sdots), among others. Such materials exhibit unique properties that lend themselves to applications in energy storage, bioimaging, catalysis, and antimicrobial formulations.[22–29]

The significance of sulfur-based materials extends beyond their intrinsic properties. Their synthesis aligns closely with the principles of green chemistry, addressing global challenges such as environmental pollution, resource conservation, and energy efficiency.[30] Mechanochemical transformations of sulfur thus hold the potential to address two critical issues simultaneously: the utilization of an abundant industrial byproduct and the sustainable synthesis of advanced functional materials. This review provides a comprehensive exploration of the mechanochemical conversion of elemental sulfur into sulfur nanomaterials. It delves into the fundamentals of mechanochemical processes, highlights recent advancements in sulfur-based nanostructures, polymers, and composites, and discusses their potential applications across various scientific and industrial domains. Furthermore, the review identifies current challenges and emerging opportunities, aiming to inspire further research in this rapidly evolving field. By integrating mechanochemistry with sulfur chemistry, this field has the potential to redefine sustainable materials design and utilization for the modern world.

2. Mechanochemistry: an overview

The resurgence of mechanochemistry as a central synthetic strategy in materials chemistry has fundamentally reshaped our understanding of material transformation. Far from being a crude method of grinding materials together, modern mechanochemistry offers a powerful and precise alternative to classical thermal or solution-based routes. This section explores and examines the mechanistic foundations, historical context, and evolving role of mechanical force in nanomaterials synthesis, providing a foundation for its application in the design of sulfur-based nanostructures.

2.1 From thermal activation to mechanical reactivity

In conventional synthetic chemistry, thermal activation serves as the fundamental driving force behind reaction design. According to the Arrhenius framework, heating enhances both the frequency and energy of molecular collisions, enabling

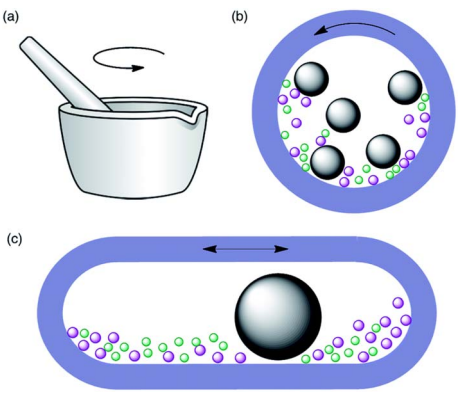

Fig. 1 Schematic representations of the three main modes of mechanical activation of chemical reactions: (a) grinding with a mortar and pestle, (b) planetary ball milling; (c) high-speed vibration milling in a mixer mill. Reproduced from ref. 79 with permission from Royal Society of Chemistry, copyright 2018.

systems to overcome energy barriers and reach the transition state.[31,32] While effective, thermal activation is inherently indiscriminate: it excites all degrees of freedom and often requires high temperatures, solvents, or catalysts, thereby increasing energy consumption and the risk of side reactions.

Mechanochemistry offers a fundamentally different approach for driving chemical reactions. The chemical reactions are initiated by the direct application of mechanical force, through grinding, milling, shearing, or stretching (Fig. 1). This mechanical input induces localized stress that perturbs atomic arrangements, alters orbital overlaps, and destabilizes crystal lattices.[33,34] As a result, it enables an alternative, non-thermal pathway to chemical reactivity. Unlike uniform thermal excitation, mechanochemical activation is spatially localized and temporally intermittent, leading to unique reaction environments and often yielding distinct products.

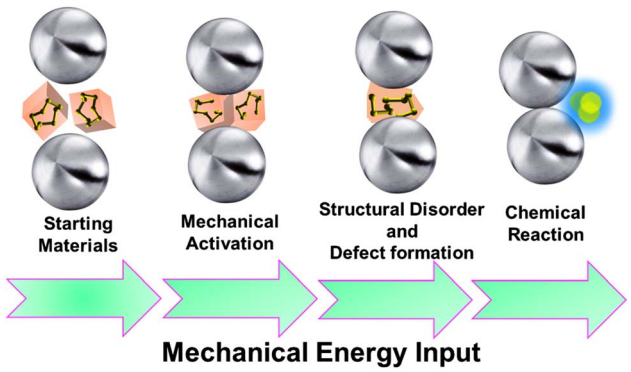

Fig. 2 Formation of products from reactants using mechanochemical synthesis.

2.2 Historical evolution and rise of mechanochemistry

Although mechanical processing has ancient roots in metallurgy and mineral extraction, its recognition as a tool for inducing chemical transformations dates to the early 20th century.[35] Pioneers like Ostwald and Carey Lea first observed chemical changes in solids subjected to mechanical force.[36,37] However, the field remained largely underexplored until the late 20th century, when advances in ball milling technology and growing interest in solvent-free, green chemistry began to catalyze renewed attention. At present, mechanochemistry is a well-established strategy across multiple disciplines, including pharmaceutical co-crystals, polymers, metal–organic frameworks and inorganic nanomaterials.[38,39] The development of high-energy ball mills, twin-screw extruders, and *in situ* monitoring techniques has been further cemented as both a practical tool and a conceptually rich approach (Fig. 3).[40,41]

2.3 Mechanochemical activation and its electronic consequences

Mechanical force interacts with solids at the atomic level in ways that are not mirrored in thermal systems. By breaking symmetry, distorting bond angles, and altering interatomic distances, mechanical input can reshape the electronic structure of materials (Fig. 2). In some cases, this leads to transient orbital mixing or electronic degeneracy, an effect similar to an inverse Jahn–Teller distortion, thereby lowering the HOMO–

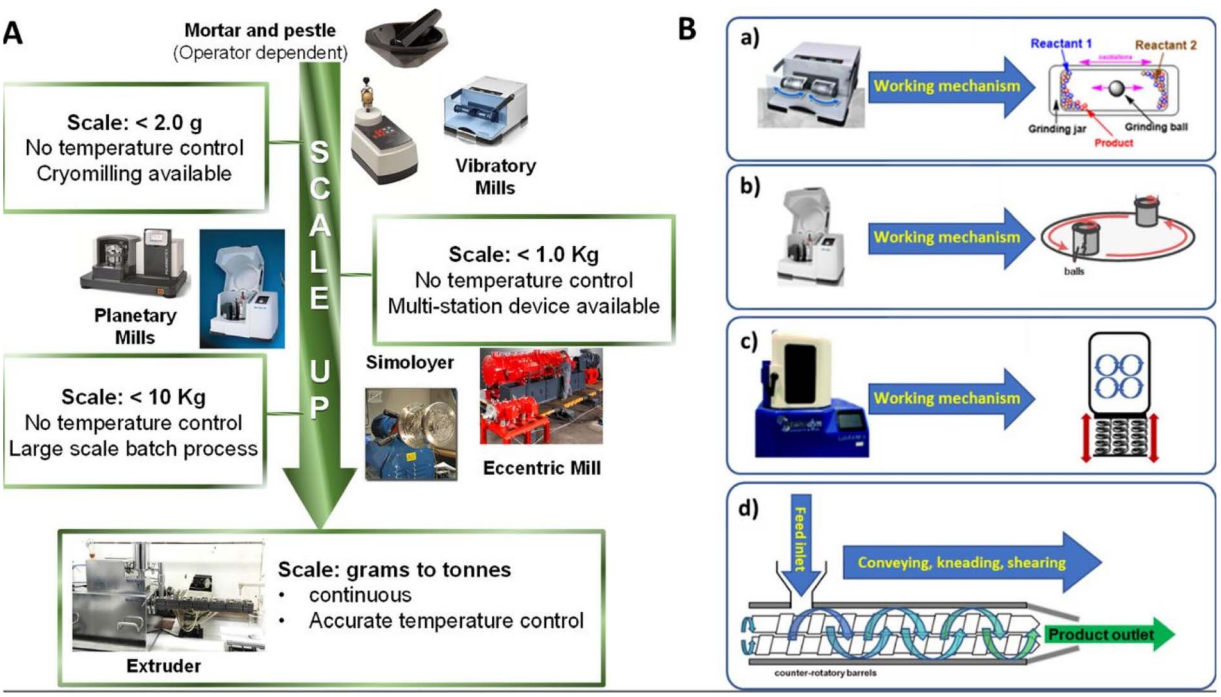

Fig. 3 (A) Schematics for mechanochemical scaling from the mortar to the twin-screw extruder; (B) mechanochemical tools with their mechanism: (a) vibratory shaker mill, (b) planetary mill, (c) resonant acoustic mixer, (d) twin-screw extruder. Reproduced from ref. 42 with permission from Wiley-VCH, copyright 2023.

LUMO gap and enhancing reactivity.[43–45] These effects have been observed in diverse systems, from stretched single molecules to energetic crystals like FOX-7 and LiN_3.[46,47] Importantly, mechanochemical reactions often yield metastable or defect-rich products that reflect kinetic rather than thermodynamic control. This is especially relevant in the synthesis of nanomaterials, where defect structures, grain boundaries, and amorphous domains strongly influence properties. Evidence from ball-milling experiments, such as prolonged milling of Fe–Cr–Si alloys, shows pronounced broadening and eventual disappearance of XRD peaks, indicating significant structural disorder, grain refinement, and dislocation formation.[48] Such structural transformations are central to mechanochemical activation mechanisms. Further insights come from *in situ* synchrotron X-ray diffraction studies of mechanochemical ZnS synthesis, where milling induced sulfur sublimation and the temporary formation of metastable hexagonal ZnS (wurtzite) before its conversion to the more stable cubic phase.[49] These observations imply that mechanical collisions and defect generation create conditions for non-thermal bond rearrangements. Additionally, in polymer systems, mechanical force can cleave covalent bonds, including C–S bonds, resulting in radical species that drive further transformations.[50] Though harder to detect in sulfur-only systems, this general principle suggests that radical intermediates may form during mechanochemical processing as well. These validated observations support a mechanistic model for sulfur systems in which shear, stress, and impact lead to localized defect generation, electronic redistribution, and bond cleavage. This pathway is distinct from thermal or solution-phase sulfur chemistry and forms the mechanistic basis for many mechanochemically synthesized materials.

2.4 Defect engineering and energy storage in solids

A defining feature of mechanochemistry is its ability to generate and manipulate lattice defects. When subjected to mechanical stress, crystalline solids accumulate strain energy that manifests as point defects, dislocations, and amorphous regions. These features are not merely structural by-products, they play an active role in reaction kinetics, phase transformations, and diffusion pathways.[51,52] During high-energy grinding, materials undergo microplastic deformation and localized stress, particularly at dislocation cores and crack tips. These regions often serve as nucleation sites for chemical reactions, characterized by altered electronic structures and enhanced mass transport properties. Furthermore, defect-rich zones store potential energy that can later be released through processes such as annealing or recrystallization, thereby contributing to product evolution over time.[53,54] For instance, sulfur, when subjected to mechanochemical treatment, undergoes not only crystalline distortion but also partial amorphization that increases reactive surface area and exposes under-coordinated sulfur atoms. The generation of high-energy defect-rich zones has been shown to facilitate sulfur–metal interactions in hybrid composites, as seen in Zn–S and Bi–S systems prepared *via* mechanochemistry.[55] Such regions act as both electron donors and trapping sites, making them central to redox-active applications in photocatalysis or batteries. Surface effects are especially critical as mechanochemical transformations typically initiate at or near the particle surface.[56] The altered microstructure and bonding in these near-surface regions govern initial reactivity and influence the accessibility of reactive intermediates. In many nanomaterial systems, including sulfur-based nanomaterials, surface phenomena determine final particle size, morphology, and stability.

2.5 Mechanophores and emerging characterization tools

A novel extension of mechanochemistry involves the use of mechanophores, molecular motifs that respond to mechanical force with visible changes in properties such as color or fluorescence.[57] These are increasingly used as *in situ* probes of force distribution during polymer deformation or solid-state processing. Simultaneously, recent advances in real-time characterization methods such as time-resolved X-ray diffraction (XRD), Raman spectroscopy, and synchrotron-based imaging, have begun to illuminate the transient processes and intermediates generated during mechanochemical treatment.[58–60] Although many defect structures remain elusive due to their short lifetimes, the evolving toolkit is rapidly expanding our understanding of these complex systems. This is particularly relevant in sulfur-based systems where intermediate states, like short-chain polysulfides or semi-amorphous allotropes, exist briefly and are difficult to capture post-reaction. While direct *operando* tracking of S–S bond cleavage is still evolving, indirect markers (*e.g.*, peak shifts in Raman and UV-vis, ESR detection of radicals) offer promising avenues for decoding these transformations.

2.6 Mechanochemistry in elemental sulfur activation

Elemental sulfur, characterized by its stable allotropes and strong covalent S–S bonds, presents a synthetic challenge under ambient conditions. However, mechanical activation offers a viable pathway to disrupt S_8 rings, initiate polymerization, and transform crystalline sulfur into amorphous, chain-like, or nanostructured forms. This transformation is enabled by shear-induced bond distortion and the generation of surface defects, often working in synergy with dopants, metal salts, or carbon-based templates. The inert nature of sulfur under grinding conditions becomes dynamically reactive, enabling reaction pathways that are typically inaccessible *via* thermal or solution-based methods. A comparative framework underscores this contrast: thermal methods rely on random, uniform excitation, whereas mechanochemical activation imparts localized shear and compressive stress. This leads to site-selective bond scission and initiation of radical or nucleophilic chain propagation.[61] These findings are consistent with the broader mechanistic understanding of mechanically triggered redox chemistry in chalcogenides and validate the unique pathway sulfur follows under grinding conditions. The resulting nanostructured sulfur materials display properties that are highly dependent on defect density, surface reactivity, and kinetic

trapping. All of these properties are inherently linked to the mechanical history of the system.

2.7 Mechanochemical sulfur doping and hybridization

Recent advances have demonstrated that mechanochemistry is a powerful method for doping sulfur into carbonaceous frameworks or forming sulfur-containing hybrid nanomaterials with structural control. Under high-energy milling, the reactive environment facilitates substitutional doping, interfacial hybridization, and molecular integration of sulfur with π-conjugated systems, polymers, or heteroatom scaffolds. This doping often occurs alongside nitrogen or other heteroatoms, exploiting synergistic effects to tune electronic structure, conductivity, and redox behaviour, key for applications in energy storage, catalysis, and environmental remediation.

Hao *et al.* recently reported the co-doping of nitrogen and sulfur into γ-graphyne through a bottom-up mechanochemical strategy, forming quasi-pyridinic N/S-doped structures that significantly enhanced Li-ion storage capacity (up to 1003 mA h g^{-1} after 150 cycles) and lithium-ion diffusion (2.6×10^{-12} cm^2 s^{-1}).[62] The synergistic effect of N and S atoms facilitated channel formation and electron cloud modulation, enabling improved Li^+ mobility through alkynyl-rich domains.

A similarly elegant approach by Li *et al.* demonstrated the *in situ* synthesis of S-doped alkynyl carbon materials (SACM) *via* co-milling hazardous endosulfan with CaC_2. The reaction not only decomposed the persistent pollutant cleanly but also yielded a high-performance supercapacitor electrode (232.3 F cm^{-3}) and an efficient Hg(II) adsorbent (675.7 mg g^{-1}), showcasing the potential of multi-functional materials derived from green mechanochemical reactions.[63]

Another green protocol enabled S-doped graphyne formation from tetrabromothiophene and CaC_2, again *via* solvent-free milling. The resulting material possessed a thienyl–alkynyl carbon skeleton with hierarchical porosity and demonstrated excellent performance in both Hg(II) removal (869.6 mg g^{-1}) and electrochemical energy storage (415.6 F cm^{-3}), highlighting the dual functionality of sulfur dopants in regulating adsorption and conductivity.[64]

Lee *et al.* employed sulfur black dye and graphite to mechanochemically produce dual-doped porous carbon materials for lithium/sodium-ion battery anodes. The resulting electrodes achieved high rate capability (672 mA h g^{-1} at 0.1 A g^{-1}) and strong cycle performance due to the abundant active sites and enhanced electrochemical kinetics from sulfur and nitrogen dopants.[65]

Earlier, Yuasa *et al.* introduced N and S dual doping in multilayer graphene using thiourea and urea under ball-milling, producing a bifunctional electrocatalyst with strong ORR and OER activity. The heteroatom synergy introduced *via* mechanical activation improved reaction selectivity and catalytic activity significantly.[66]

Altogether, these studies show that mechanochemistry not only activates elemental sulfur but also enables precise doping and hybridization with various carbon forms. This opens new fields in the synthesis of compositionally and functionally diverse sulfur-based materials. While these studies highlight the broader potential of mechanochemistry in sulfur doping and hybridization, the main focus of this review is specifically on sulfur-based nanomaterials where sulfur is the principal component and the defining contributor to the material's properties. The following section explores specific protocols and strategies for the mechanochemical synthesis of sulfur-based nanomaterials.

3. Mechanochemical synthesis of sulfur nanomaterials and formation mechanism

This section aims to provide an overview of the various mechanochemical synthetic approaches for the preparation of sulfur nanomaterials and sulfur nanodots. In 2015, Urakaev *et al.* proposed the mechanochemical synthesis method of the elemental SNP or the nanodispersed sulfur (S_n^0) in the matrix of sodium sulfite and succinic acid.[22] The formation of SNPs occurs *via* the following reaction.

$$Na_2S_2O_3 \cdot 5H_2O + H_2(C_4H_4O_4) + zNa_2SO_3 = (z+1)Na_2SO_3 + H_2(C_4H_4O_4) + 5H_2O + S_n^0, \text{ (at } z = 19.6)$$

The nanosulfur was formed by the decomposition of the highly unstable thiosulfuric acid intermediate. The mixture of sodium sulfite and succinic acid was subjected to mechanical activation in the Pulverisette planetary-type ball mill for different periods and different rotation rates. The product so obtained was removed from the cylinder and washed with water, followed by centrifugation. The product was then dried to obtain the SNPs. Subsequently, a similar synthetic approach for SNPs was reported by Islamov and co-workers.[23] In this work, the SNPs underwent post-treatment to form a stable SNP solution. The SNPs were precipitated and washed with ethyl alcohol. Then the SNPs was suspended in a surfactant solution and subjected to ultrasound treatment for 20 minutes resulting in a stable SNP suspension.

Furthermore, SNPs were also synthesized using a mechanochemical approach on the substrate materials reported by Ma *et al.* (Fig. 4). They synthesized ultrafine sulfur particles *via* high-energy ball-milling. These particles were anchored onto *in situ* exfoliated graphene with the assistance of dielectric barrier discharge (DBD) plasma.[24] A mixture of 325-mesh graphite and sulfur powder, in a 3 : 7 mass ratio, was ground together and subjected to high-energy ball milling. This process was simultaneously assisted by DBD plasma for 3 hours at an electric current of 1.5 A. As a result, ultrafine SNPs were formed and anchored onto the exfoliated graphene, producing a composite named S/G-DBD. To investigate the influence of DBD plasma, several controlled samples were synthesized. The synthesis duration was varied, resulting in samples named S/G-DBD2 and S/G-DBD5, corresponding to 2 and 5 hours of processing time, respectively. Additional samples were prepared with a synthesis time of 3 hours but with different sulfur contents – 60% and

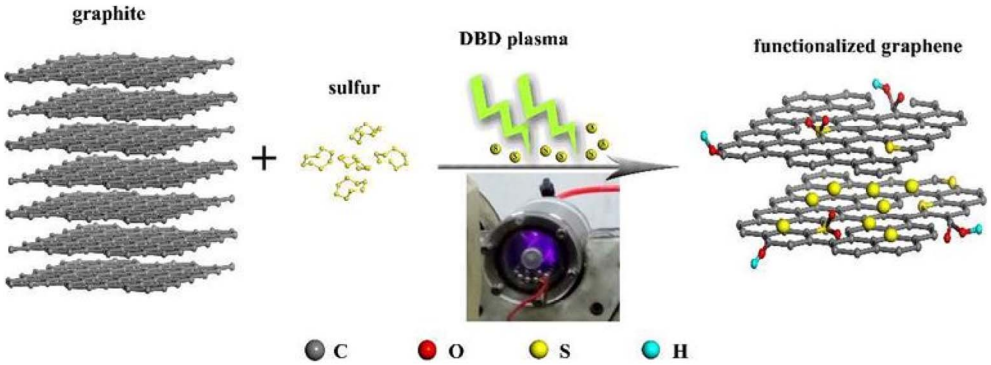

Fig. 4 Representation of the synthesis of a sulfur/graphene composite by a one-pot ball milling technique. Reproduced from ref. 24 with permission from Royal Society of Chemistry, copyright 2017.

80% – to study the effect of sulfur concentration. A control sample, referred to as S/graphite, was also synthesized using the same method as for S/G-DBD but without the application of DBD plasma. Furthermore, graphite was ball-milled for 3 hours both with and without DBD plasma in the absence of sulfur powder. These samples, named G-DBD and G respectively, were used to evaluate the effect of DBD plasma on enhancing the specific surface area. In another study, Siqi Qi *et al.* reported the synthesis of an SNP composite with unzipped multi-walled carbon nanotubes (S@UMWNTs) *via* ball milling.[25] Unzipped multi-walled carbon nanotubes and sulfur were mixed in a 3 : 7 ratio in a stainless-steel capsule filled with argon gas. The capsule was then mounted on a planetary ball mill and processed for 24 hours at 480 rpm resulting in the formation of the S@UMWNT composite.

Mechanochemistry has also been employed in the synthesis of SNPs using surfactant mixtures, as reported by Turganbay *et al.*[26] The synthesis was carried out in two stages. In the first stage, 10 grams of crystalline bulk sulfur was milled for approximately 30 minutes which produced sulfur powder with particle sizes ranging from 10 to 100 microns. In the second stage, the milled sulfur powder was ultrasonicated in a 100 mL aqueous solution containing water-soluble polyelectrolyte/surfactant mixtures—specifically, 1 mM MC/CTAB with PDADMAC/SDBS, and 0.1 mM NaCMC/Triton X-100 which resulted in further reduction of sulfur particle size and formation of SNPs. A similar approach was reported again by Turganbay *et al.* for the synthesis of SNPs.[27] Firstly, 10 g of the crystalline sulfur was milled for 3 min which produced 50–60 micron sulfur powder. In the next step, 100 mL of the aqueous surfactant solution (containing 0.36 mM SDBS, 1.0 mM CTAB and 0.24 mM TX-100) was used to disperse the sulfur powder obtained from milling. The resultant suspension was subjected to ultrasonication for 10 min at 60% amplitude corresponding to an energy input of 367 J cm^{-3}. To minimize heat generation, a 2 second on/off pulse cycle was applied, resulting in a post-treatment suspension temperature of approximately 50 °C. The crushed sulfur was then dried using a freeze-dryer. The experiment was repeated three times to ensure reproducibility and to yield SNPs.

Interestingly, current research trends are revitalizing the role of mechanochemistry taking it to the next level by enabling the design and synthesis of advanced sulfur nanomaterials.[39,57] Departing from classical organic synthesis methods, mechanochemistry has also been successfully applied to synthesize sulfur quantum dots (Sdots).[28] The mechanochemical approach was employed for the first time to synthesize a new member of the nanosulfur family *i.e.* Sdots by Arshad *et al.* using sodium thiosulphate as the precursor (Fig. 5). In this method, NaOH was first ground into a fine powder to form a moist paste in a mortar and pestle, to which sodium thiosulfate and oxalic acid were added and further ground. Subsequently, PEG-400 was introduced into the reaction mixture, and grinding was continued for an additional 10–15 minutes. As grinding progressed, the color of the mixture changed from light yellow to white powder, indicating the formation of Sdots. The product was then purified by dialysis for 1 hour which yielded fluorescent Sdots with a quantum yield of 4.8%. This method significantly reduced the reaction time from several hours to less than one hour. In this process, elemental sulfur was first produced by the reaction between sodium thiosulfate and oxalic acid. Subsequently, Na_2S was partially formed *via* the reaction between NaOH and the *in situ*-generated elemental sulfur. A short-chain polymerization reaction between sulfur and Na_2S then led to the formation of Sdots. Notably, PEG-400 served as both a passivating and stabilizing agent throughout the synthesis. The mechanochemical synthesis pathway of Sdots is demonstrated by the reactions below.

$$Na_2SO_3 + C_2H_2O_4 = Na_2C_2O_4 + SO_2 + S\downarrow + H_2O \quad (1)$$

$$SO_2 + H_2O = H_2SO_3 \quad (2)$$

$$3S + 6NaOH = 2Na_2S + Na_2SO_3 + 2H_2O \quad (3)$$

$$(x - 1)S + Na_2S = Na_2S_x \text{ (where } x = 2\text{–}6) \quad (4)$$

To eliminate the possibility of fluorescence arising from any impurities, several control experiments were conducted. None of these experiments showed any evidence of emission at λ_{ex} =

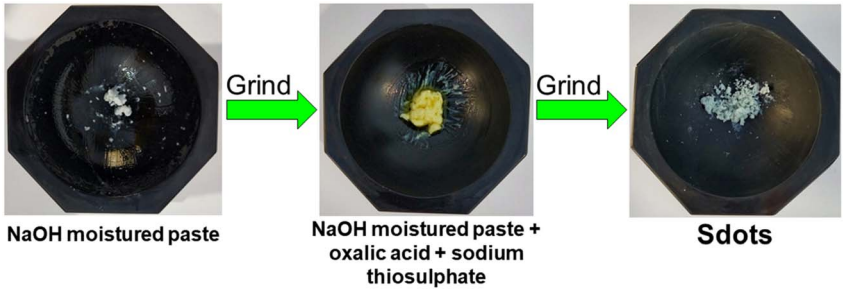

Fig. 5 Illustration of the steps involved in the mechanochemical synthesis of fluorescent Sdots using a mortar and pestle for grinding. Reproduced from ref. 28 with permission from American Chemical Society, copyright 2021.

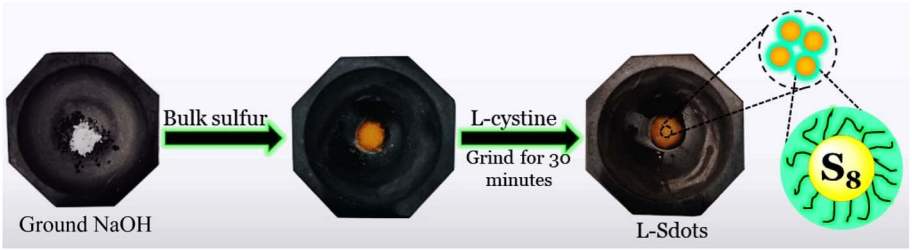

Fig. 6 Illustration of the steps involved in the mechanochemical synthesis of luminescent, chiroptically active L-Sdots using elemental sulfur. Reproduced from ref. 29 with permission from American Chemical Society, copyright 2024.

360 nm. These control experiments indicate that no fluorescent impurities were formed during the synthesis process of Sdots.

Recently, Hasan and co-workers have also reported the mechanochemically driven synthesis of Sdots.[29] By them, an efficient synthetic method of Sdots from the earth-abundant elemental sulfur using the mechanochemical synthetic technique was developed (Fig. 6). In this work, chiroptically active Sdots were synthesized using the biomolecule cysteine and sulfur powder. The biomolecule cysteine plays a key role in inducing chirality in the Sdots. For the synthesis of L-Sdots, NaOH was ground to get a moist paste, after which sublimed sulfur powder and L-cysteine were added. The resulting mixture was thoroughly ground using a mortar and pestle for 30 minutes, during which mechanical activation facilitated the formation of chiral Sdots. A similar procedure was followed for the synthesis of D-Sdots where D-cysteine was replaced by L-cysteine. For both L- and D-Sdots, the crude products were diluted with double-distilled water and ground further. To purify the chiral Sdots, the reaction mixture was centrifuged at 6000 rpm for 20 minutes. The clear supernatant was separated from the solid residue and subsequently dialyzed in distilled water for 24 hours to ensure complete purification. The purified L-Sdots exhibited a quantum yield of 14.6%. Purification is an essential step in the synthesis of L-Sdots as it eliminates ionic and molecular contaminants from the reaction mixture. To rule out the possibility of fluorescence arising from impurities, several control experiments were conducted. In the first set of experiments, the order of reagent addition was altered from the standard synthesis protocol. The sublimed sulfur powder was first ground followed by the addition and grinding of L-cysteine. NaOH was then introduced to the mixture and ground for 30 minutes. However, no fluorescence was observed at an excitation wavelength of $\lambda_{ex} = 365$ nm. In the second set, sublimed sulfur powder was not used during the synthesis and no emission was detected from the reaction product at $\lambda_{ex} = 365$ nm. In the third set, L-cysteine was excluded from the original sequence which resulted in no fluorescence at the same excitation wavelength. In the fourth set, NaOH was not added in the original synthesis method and similarly, no emission was observed at $\lambda_{ex} = 365$ nm. These observations confirm that no fluorescent impurities were formed during the synthesis and that all three components – NaOH, sulfur powder, and cysteine – are essential for the formation of chiral Sdots.

4. Structural characteristics

4.1 Morphology

Transmission electron microscopy (TEM) was employed to examine the size and morphology of the sulfur nanomaterials. Urakaev *et al.* reported the size of mechanochemically activated SNPs to be in the range of 20–80 nm.[22] Similarly, Arshad *et al.* synthesized PEG-stabilized Sdots and observed an inhomogeneous size distribution with an average particle size of 9.88 ± 2.10 nm (Fig. 7a).[28] The Sdots formed were not perfectly spherical but exhibited a quasi-spherical shape. High-resolution TEM (HRTEM) analysis of the Sdots revealed lattice fringes of 0.21 nm and 0.25 nm corresponding to the (337) and (244) crystal planes of sulfur, respectively (Fig. 7b). Hasan *et al.* also reported quasi-spherical Sdots with average sizes of 7.59 ± 3.24 nm for L-Sdots and 4.92 ± 1.6 nm for D-Sdots.[29] In another work, SEM analysis confirmed the formation of SNP with an average size of nearly 100 nm.[22] For hydrophilic SNPs, SEM

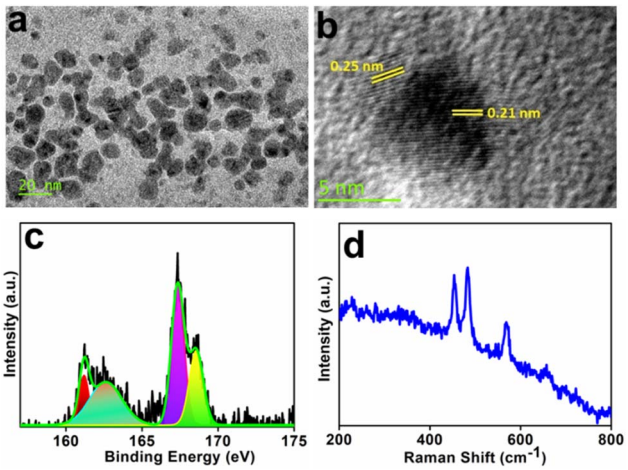

Fig. 7 (a) TEM image of the Sdots, (b) HRTEM image showing the observed *d*-spacing in Sdots, (c) deconvoluted high-resolution XPS spectrum of the S_{2p} region, (d) Raman spectrum of Sdots. Reproduced from ref. 28 with permission from American Chemical Society, copyright 2021.

images showed spherical morphology, with smaller particles aggregating into larger structures ranging from 150–200 nm in size.[27]

4.2 Chemical bonding

The elemental composition and chemical bonding of sulfur nanomaterials are typically analyzed using X-ray photoelectron spectroscopy (XPS) and Raman spectroscopy. The XPS spectrum of S@UMWNTs exhibited a peak at 285.5 eV corresponding to the C–S bond.[25] This bond arises from radicals generated during the mechanochemical cleavage of weaker S–S bonds in sulfur, which subsequently react with C=C bonds and oxygen-containing functional groups. Arshad *et al.* recorded the high-resolution XPS spectrum of the S_{2p} region in Sdots, and the deconvoluted spectrum revealed four distinct peaks at 161.2, 162.6, 167.3, and 168.5 eV (Fig. 7c).[28] The peaks at 161.2 and 162.6 eV were attributed to atomic sulfur, while the peaks at 167.3 and 168.5 eV corresponded to oxidized sulfur species such as sulfate and sulfite groups. Similarly, Hasan *et al.* reported peaks at 161.5 and 162.9 eV for atomic sulfur in L-Sdots, along with a peak at 164.0 eV attributed to unbound disulfide bonds in L-cystine, *i.e.*, divalent sulfur ions $(S_2)^{2-}$ (Fig. 8a).[29] Additional deconvoluted peaks at 167.8 and 169.1 eV were assigned to oxidized forms of sulfur, such as SO_3^{2-} and SO_2^{-}.[29]

Raman spectroscopy was also employed as an effective tool to confirm the formation of Sdots. The Raman spectrum of Sdots showed three prominent peaks at 453.5, 483.2, and 569.4 cm^{-1} (Fig. 7d).[28] The peaks at 453.5 and 483.2 cm^{-1} correspond to the S–S stretching vibrational modes of zero-valent atomic sulfur, while the peak at 569.4 cm^{-1} is associated with polysulfide species (S_4^{-} and S_5^{-}), indicating polymerization of sulfur. In another study, the Raman spectrum of L-Sdots exhibited peaks at 153, 219, and 474 cm^{-1}, which were also attributed to S–S stretching modes.[29] These findings collectively suggest the formation of polymeric sulfur within the core of the Sdots.

4.3 Structure

Powder X-ray diffraction (PXRD) analysis of SNPs confirmed the presence of monophase sulfur in the orthorhombic α-S_8 form.[22,26,27] PXRD studies further indicated the crystalline nature of the Sdots.[28] Similarly, the diffraction pattern of L-Sdots also revealed the presence of the orthorhombic α-S_8 phase.[29]

To gain deeper insight into defect states, electron paramagnetic resonance (EPR) spectroscopy was performed at room temperature. In the case of L-Sdots, a broad signal centred at $g = 2.1$ was observed, indicating the presence of sulfur vacancies (Fig. 8b).[29] These defect species are attributed to vacancy sites located at the edge of the sulfur core.

Notably, the combined results from XRD, Raman, and XPS analyses indicate that the sulfur nanomaterials such as Sdots consist of a polymeric sulfur core.

4.4 Surface functionalities

Fourier transform infrared (FTIR) spectroscopy was employed to gain insight into the surface functional groups. In the case of PEG-stabilized Sdots, characteristic vibrational bands in the FTIR spectra of both Sdots and PEG-400 were found to be similar which suggests the absence of any chemical interaction between them. This indicates that PEG-400 acts solely as

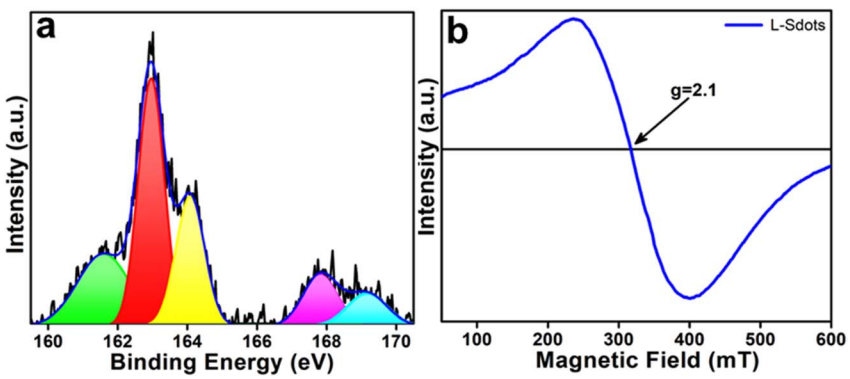

Fig. 8 (a) Deconvoluted high-resolution XPS spectrum of the S_{2p} region of L-Sdots, (b) EPR spectrum of L-Sdots recorded at room temperature. Reproduced from ref. 29 with permission from American Chemical Society, copyright 2024.

a stabilizing and capping agent.[28] The FTIR spectrum of L-Sdots exhibited both a shift and change in the shape of characteristic peaks compared to pure L-cysteine which indicates the chemical interaction between the functional groups and the sulfur core of L-Sdots.[29] This observation confirms that the surface of the polymeric sulfur core is stabilized and capped by L-cysteine, rather than being a direct result of the reaction precursor alone. Furthermore, ^{1}H NMR analysis supports this conclusion and reveals that the surface of L-Sdots is capped by L-cysteine, while D-Sdots are capped by D-cysteine.[29] Notably, due to the nanoscale size of the Sdots, homogeneous broadening around ~3.2 ppm was observed in the ^{1}H NMR spectrum of L-Sdots.

5. Optical characteristics

5.1 Absorption

Sdots primarily exhibit absorption in the ultraviolet region. The UV-vis absorption spectrum of Sdots displays three prominent peaks centred at 212, 322, and 402 nm (Fig. 9a). The peak at 212 nm is attributed to the n → σ* transition which arises from heteroatoms present on the surface of the Sdots. A similar peak was reported at 250 nm by Hasan *et al.* corresponding to the same transition involving non-bonded sulfur electrons (n → σ*).[28,29] The absorption bands at 322 nm and the broader band at 402 nm are attributed to polysulfide species such as S_6^{2-} and S_4^{2-} which further indicates the presence of polymeric sulfur structures within the Sdots. These polymeric sulfur structures are also evident from the Raman spectrum which showed the presence of polysulfide species (S_4^- and S_5^-).[28]

5.2 Photoluminescence (PL) and optical stability

Since Sdots are still in the early stages of development, the origin of their characteristic PL remains largely unexplored and requires further investigation. Notably, their emission behavior is distinctly different from that of other sulfur-based nanomaterials. The advancement of conventional sulfur SNPs has been limited due to their low reactivity and relatively large particle size, which hinders their potential applications. In contrast, Sdots displayed good PL quantum yield and tunability in excitation-dependent emission. The photoluminescent quantum yield of Sdots prepared using acid etching oxidation, assembly fission, and hydrothermal and *in situ* reactions ranges from 0.549% to 10.3%.[67–73] Also, the microwave irradiation method and the oxygen accelerated technique when combined with various passivating agents have been reported to produce Sdots with significantly higher QY up to 49.25%. However, it is possible that the use of these passivating agents at elevated temperatures may have led to the formation of nanofluorophores, which could contribute to the observed high fluorescence. To address concerns regarding fluorescent impurities, Hasan reported the mechanochemical synthesis of L-Sdots with a QY of 14.6% and conducted control experiments to rule out contributions from such impurities to the PL of the Sdots.[29] Arshad *et al.* recorded the PL spectra of Sdots in the range between 350 nm and 450 nm and they exhibit excitation dependent emission spectra (Fig. 9b).[28] A noticeable red shift in the emission maximum was observed with shifting from 455 nm to 532 nm as the excitation wavelength increased from 350 nm to 450 nm. The maximum emission intensity for the Sdots was observed at 461 nm when excited at 363 nm (Fig. 9c).

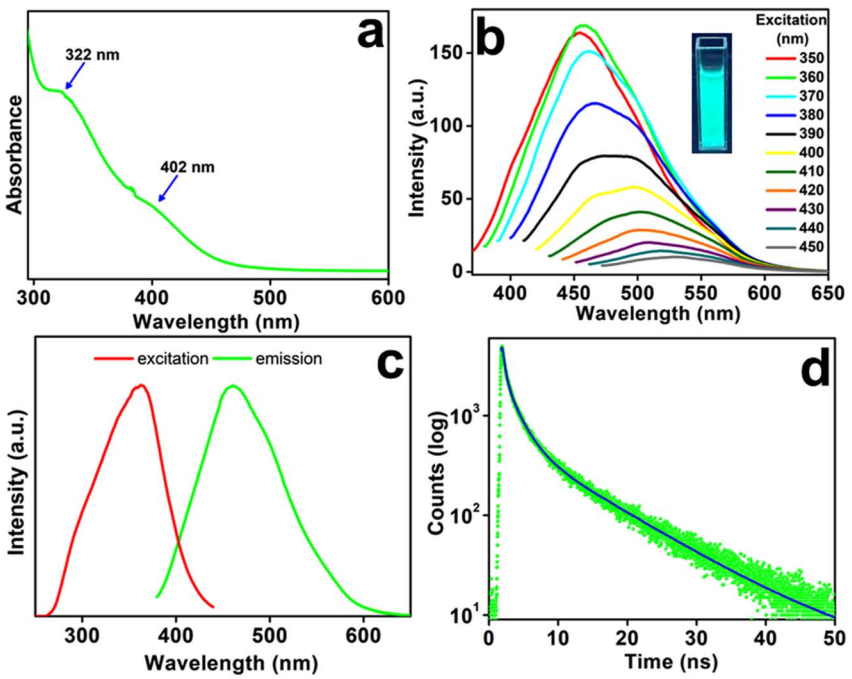

Fig. 9 (a) UV-visible absorption spectrum of Sdots. (b) PL spectra of Sdots in an excitation wavelength range from 350 nm to 450 nm depicting excitation wavelength-dependent characteristic features of Sdots. (c) Corresponding excitation spectrum of Sdots for the emission wavelength maximum of 461 nm. (d) TRPL spectrum of Sdots. Reproduced from ref. 28 with permission from American Chemical Society, copyright 2021.

This excitation-dependent photoluminescence behavior is likely attributed to the inhomogeneous size distribution of the Sdots. This inhomogeneous size distribution was also observed in TEM images with the morphology of Sdots being quasispherical instead of perfectly spherical. To evaluate their optical stability, time-dependent PL measurements were conducted after exposing the Sdots to UV light. Remarkably, the photoluminescence intensity remained unchanged even after prolonged exposure which demonstrated the excellent optical stability of the Sdots.

In another work, Hasan *et al.* also reported excitation-dependent emission spectra with a minor red shift in the emission maxima from 445 nm to 465 nm when excitation wavelength increased from 340 nm to 420 nm.[29] However, when the excitation wavelength changed from 360 nm to 400 nm, a trivial red shift from 450 nm to 458 nm was observed. This negligible red shift in the excitation-dependent emission spectra of Sdots excludes the origin of the emission from the surface state. The normalized solvent-dependent PL spectra indicated that surface functional groups play a significant role in the emissive transitions of Sdots. Additionally, temperature-dependent PL measurements recorded in the range of 0 to 70 °C showed maximum emission intensity at 20 °C. Time-resolved PL analysis further highlighted the influence of surface trap states on emission behavior. These findings suggest that the PL of Sdots originates from the radiative recombination of photo-excited electrons from the defect states which act as traps for excitons and facilitate their migration toward surface functional groups. Moreover, photostability experiments confirmed the excellent photostability of Sdots as PL intensity remained unchanged even after prolonged exposure to UV light.

5.3 Time-resolved photoluminescence (TRPL)

TRPL measurements revealed the presence of multiple emissive sites within the Sdots. Arshad *et al.* reported a triexponential decay profile which indicates the coexistence of different emission pathways with an average lifetime of 5.9 ns (Fig. 9d).[28] The fitted lifetimes are 0.32 ns (τ_1), 1.97 ns (τ_2), and 10.31 ns (τ_3) with an amplitude of 69% (α_1), 24% (α_2), and 7% (α_3) respectively. The biexponentially fitted components have a shorter lifetime while the other one has a longer lifetime. The shorter lifetime was attributed to the radiative recombination of initially generated excitons, whereas the longer lifetime was associated with recombination events involving surface states. Similarly, Hasan and co-workers also observed a triexponential decay behavior, reporting an average lifetime of 2.93 ns for their Sdots,[29] further supporting the presence of multiple emissive states contributing to the photoluminescence mechanism.

5.4 Ground state and excited state chiroptical properties

The ground-state chiroptical properties of the Sdots were examined using the circular dichroism (CD) spectroscopic technique. Hasan *et al.* recorded the CD spectra of chiral Sdots to assess whether the structural chirality of L-cysteine was preserved in the resulting chiroptically active Sdots.[29] The CD spectra of L-Sdots and D-Sdots were found to be near mirror images of each other which exhibit two distinct peaks at 186 nm and 214 nm. The corresponding dissymmetry factors (g_{abs}) were in the range of 10^{-4} for L-Sdots and 10^{-5} for D-Sdots. These chiroptical features are attributed to the outer shell of the sulfur core which consists of the cysteine-related functionalities, thereby transferring chirality to the Sdots.

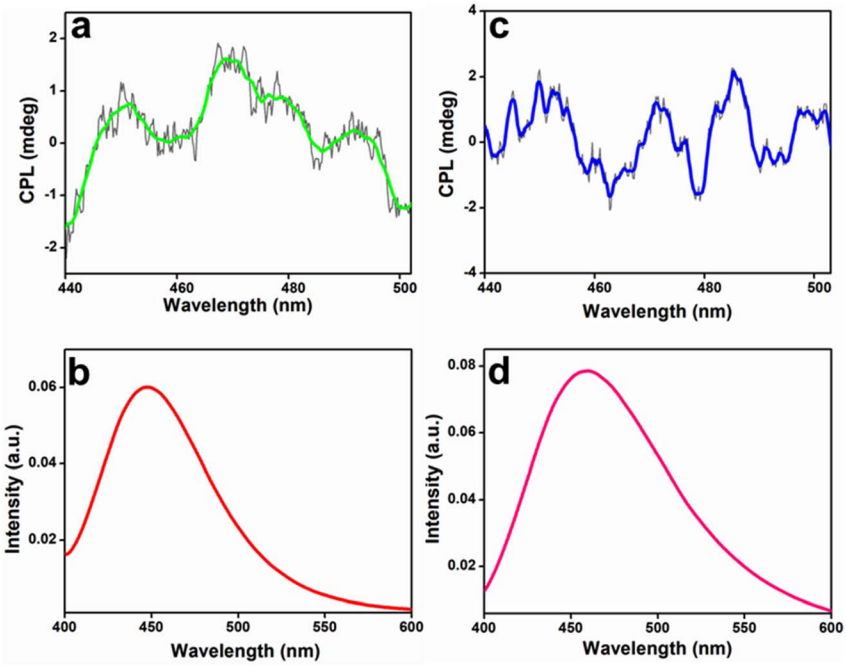

Fig. 10 (a and b) CPL spectrum and the corresponding emission spectrum of L-Sdots respectively, (c and d) CPL and the corresponding emission spectrum of D-Sdots, respectively. Reproduced from ref. 29 with permission from American Chemical Society, copyright 2024.

Excited-state chirality involves the emission of right- and left-handed circularly polarized light (CPL) which provides insight into the chiral characteristics of emissive states. Hasan *et al.* studied the excited state chiroptical properties employing CPL measurements and observed a CPL signal from L-Sdots at an excitation wavelength of 365 nm (Fig. 10).[29] The CPL emission band was centred at 467 nm which confirms the successful generation of CPL in L-Sdots. The corresponding anisotropy factor (g_{lum}), which quantifies the degree of chiral dissymmetry in fluorescence, was recorded as $+2.2 \times 10^{-3}$ at 467 nm. In contrast, no significant CPL signal was detected for D-Sdots which highlights the critical role of ligand-to-sulfur core interaction in generating excited-state chirality.

6. Applications

6.1 Electrode material in lithium–sulfur (Li–S) batteries

Sulfur has gained significant attention in Li–S batteries as an electrode material owing to its high theoretical specific capacity of 1675 mA h g^{-1}. However, due to the shuttling effect of polysulfides (Li_2S_n, $4 \leq n \leq 8$) and the insulating nature of sulfur, there has been hindrance in their practicality. However, the sulfur polymeric composites can suppress the diffusion of polysulfides by forming the C–S bond. In this regard, Siqi *et al.* had reported sulfur nanoparticles which are covalently bonded through ball milling of sulfur to unzipped multiwalled carbon nanotubes. Siqi *et al.* investigated the electrochemical performance of SNP composites (S@UMWNTs) using CR2032 coin cells.[25] The coin cells in the glovebox filled with argon were gathered with the S@UMWNTs coated with the Al foil and used as a cathode, lithium foil as a counter/reference electrode, and Celgard 3501 which is a porous membrane as the separator. After the 500 charge/discharge cycles, a small capacity decay of 0.09% was observed per cycle. The cyclic voltammetry (CV) profile of the S@UMWNTs-5 cathode was recorded over the first three cycles at a scan rate of 0.1 mV s^{-1} within a voltage range of 1.5–3.0 V *versus* Li^+/Li (Fig. 11a). Two distinct cathodic peaks were observed at 2.30 V and 2.05 V. The peak at 2.30 V corresponds to the reduction of elemental sulfur (S_8) to long-chain lithium polysulfides (Li_2S_n, where $4 \leq n \leq 8$), while the peak at 2.05 V is attributed to the further reduction of Li_2S_n to short-chain species such as Li_2S_2 and Li_2S. During the reverse scan, an anodic peak at 2.55 V was detected which corresponds to the oxidation of Li_2S_2 or Li_2S to S_8. The minimal changes in the positions of cathodic and anodic peaks over multiple cycles indicate the good electrochemical stability of the composite material.

Furthermore, the galvanostatic charge/discharge profiles of the S@UMWNTs-5 cathode were recorded from the 1st to the 100th cycle at a current density of 0.2C (Fig. 11b). During the discharge process, two voltage plateaus were observed at 2.30 V and 2.05 V which corresponds to the characteristic cathodic peaks identified in the CV curves. The voltage plateau at 2.45 V is characteristic of the anodic sweep of the CV curve. For the S@UMWNTs-5 cathode, the discharge capacity for the 1st, 10th, 30th, 50th, 80th and 100th cycles was found to be 761.6, 813.4, 781.7, 725.9, 653, and 605.7 mA h g^{-1}, respectively. Also, the S@UMWNTs-5 cathode has the highest cyclic stability with a capacity retention of 80% *i.e.* initial specific capacity of 762 mA h g^{-1} to 606 mA h g^{-1} after 100 cycles (Fig. 11c). After

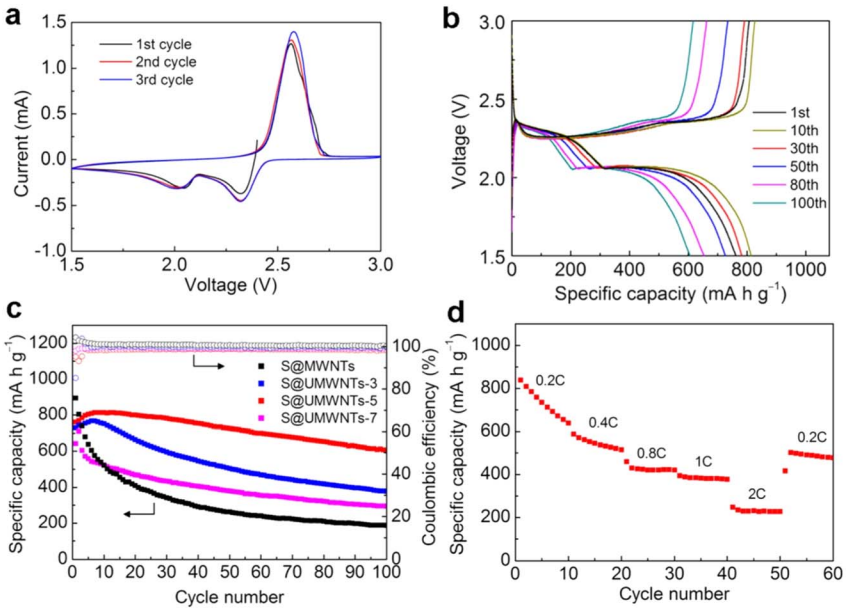

Fig. 11 Electrochemical characterization of SNP composites (S@UMWNT): (a) CV curves recorded at a scan rate of 0.1 mV s^{-1} for the S@UMWNTs-5 cathode. (b) Galvanostatic charge/discharge profiles of the S@UMWNTs-5 cathode. The current rate was 0.2C. (c) Cycling performances of S@MWNTs, S@UMWNTs-3, S@UMWNTs-5, and S@UMWNTs-7 cathodes at a current rate of 0.2C. (d) Rate performance of the S@UMWNTs-5 cathode across different current rates ranging from 0.2C to 2C. Reproduced from ref. 25 with permission from IOP Publishing, copyright 2019.

the 500 charge/discharge cycles, a small capacity decay of 0.09% was observed per cycle. Thus, the distinct cycling stabilities of S@UMWNTs-5 and S@MWNTs are due to C–S bonds in S@UMWNTs-5, which result in the suppression of polysulfide dissolution and hence the shuttling effect. Further, the rate performance of the S@UMWNTs-5 cathode was measured from 0.2C to 2C with repeated cycling, which showed the good stability and the reversibility of the S@UMWNTs-5 cathode for Li–S batteries (Fig. 11d).

6.2 Sonocatalytic dye degradation

For sonocatalytic dye degradation, sound waves of high vibrational energy during sonication were produced which result in the homolytic cleavage of molecules of water into the free radicals which are highly reactive. Addition of hydrogen peroxide further enhances the cavitation activity, leading to catalytic degradation of the organic dyes (Fig. 12). Youk and co-workers reported the synthesis of pyrrhotite NPs using ferric chloride and four different sulfur-sources, inorganic (sodium thiosulphate, sodium sulphide) and organic (thiourea, thioacetamide), having aqueous dispersibility.[74] These were designated as IS-1, IS-2, IS-3, and IS-4 respectively. The pyrrhotite NPs were synthesized *via* a wet mechanochemical method without requiring an inert atmosphere. Different sulfur sources release sulfur differently such as sodium thiosulphate upon ball-milling mechanochemically releases elemental sulfur. Thus, the different sulfur dispersing environments and the different bond energies lead to diverse polysulphide doped pyrrhotite NPs of different shapes, band gaps and sizes affecting their catalytic activity that relied on the sulphide/polysulfide ratio.

The sonocatalytic degradation efficiency of these pyrrhotite NPs was evaluated using various organic dyes such as Rhodamine B (Rh-B), Methylene Blue (MB), Methyl Orange (MO), Crystal Violet (CV), and Nile Blue (NB). The dye degradation efficiency was found to be IS-1 $\gg$ IS-2 > IS-4 > IS-3. IS-1 showed 100% removal efficiency, IS-2 was selective for MB and Rh-B, whereas IS-3 and IS-4 were found to be moderately active and inactive respectively. The reactive oxygen species $^{\bullet}OH$ by DPPH, and $^{\bullet}OH$ radical scavenging agent was identified during the sonocatalytic process. The efficiency of ROS generation corresponded with the sulfide/polysulfide ratios determined *via* X-ray photoelectron spectroscopy (XPS), measured as 3.48, 2.67, 1.29, and 1.94 for IS-1, IS-2, IS-3, and IS-4, respectively. This ratio, influenced by the mechanochemically induced sulfur environments, was identified as a key factor influencing the sonocatalytic performance during dye degradation.

6.3 Antimicrobial activity

Bulk sulfur has been known for its antimicrobial properties and it can disrupt cellular processes in microorganisms.[75–78] Bulk sulfur shows broad-spectrum activity against a variety of bacteria and fungi as it is capable of damaging cell membranes, interfering with enzyme functions, and producing reactive sulfur species that generate oxidative stress. However, the limitation of low water solubility often restricts practical applications.

Turganbay *et al.* tested the antibacterial activity of the hydrophilic SNPs for Gram-negative and Gram-positive bacteria.[27] Sulfur + SDBS was revealed to be effective against the Gram-positive bacteria *Enterococcus faecium* ATCC 700221

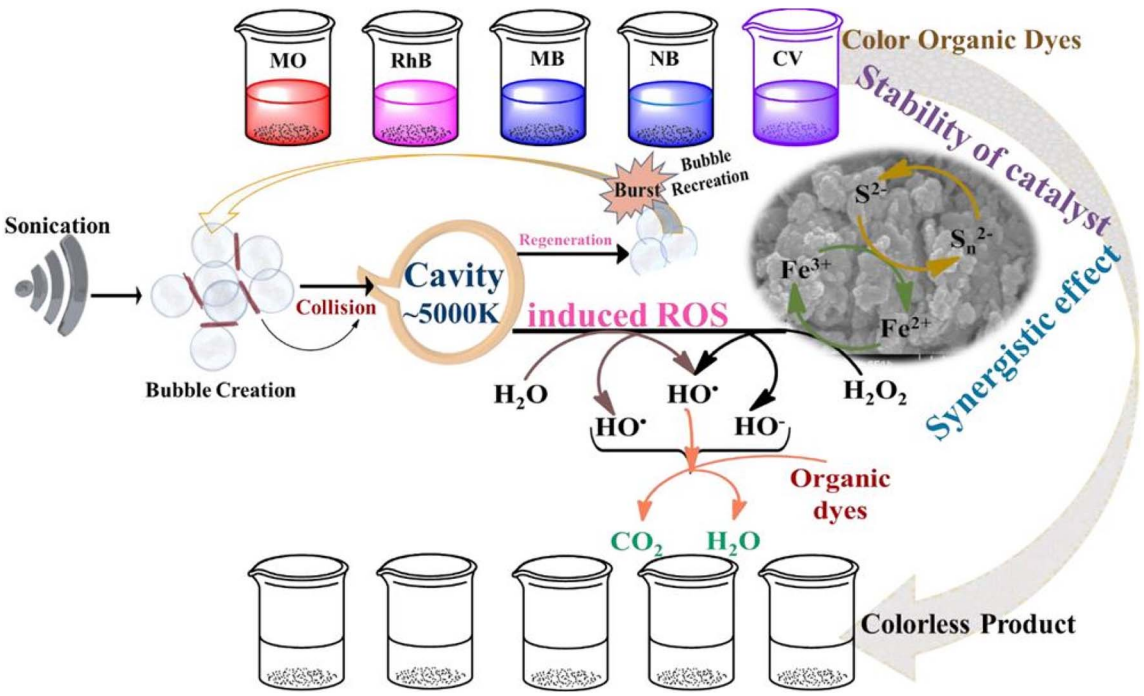

Fig. 12 Mechanism for cavitation-induced dye degradation sonochemically in the presence of mechanochemically synthesized pyrrhotite NPs. Reproduced from ref. 74 with permission from Elsevier, copyright 2022.

and *Staphylococcus aureus* ATCC 6538-P with the maximum zone of inhibition of 19.3 ± 0.58 mm and 19.0 ± 2.0 mm. Also, the antifungal effect of the sulfur + SDBS was checked against the *Aspergillus brasiliensis* ATCC 16404 and the growth inhibition zone was found to be 11.7 ± 0.58 mm. Sulfur + SDBS was found to be inactive against the Gram-negative and *Candida utilis* cells. Also, the inhibitory effect of the sulfur + CTAB was evaluated and found to be active against the Gram-negative bacteria *Klebsiella pneumoniae* ATCC with a zone of inhibition of 13.3 ± 0.58 mm, but it was found to be inactive against the other Gram-negative bacterial strains. Sulfur + CTAB was found to be active for *Staphylococcus aureus* ATCC 6538-P with a zone of inhibition value of 16.0 ± 0.0 mm, and for *Enterococcus faecium* ATCC 700221, the zone of inhibition value was 13.7 ± 0.58 mm. Also, the sulfur + CTAB antifungal effect was checked against *Candida albicans* ATCC 10231, *Candida utilis* and *Aspergillus brasiliensis* ATCC 16404; their inhibition zone was found to be 15.0 ± 0.0 mm, 22.3 ± 6.8 mm and 12.3 ± 0.58 mm respectively. Further, it was found that the sulfur + TX-100 and sulfur were inactive against all the cultures taken for the experiment. The acute toxicity was further studied to determine the toxic, tolerated and lethal dose of the hydrophilic SNPs and the cause of animal death. Doses of 50 mg kg^{-1}, 300 mg kg^{-1}, 1000.0 mg kg^{-1}, and 2000.0 mg kg^{-1} of body weight were selected and administered orally once to mice in four experimental groups. Upon physical examination, no signs of toxic damage, behavioral deviations, or changes in body weight were observed. Following planned euthanasia and according to autopsy reports, neither the relative weight coefficients of internal organs nor the absolute weight indicators showed any significant difference. Therefore, the test material was classified as non-toxic based on the observed results.

6.4 Bioimaging

The cellular biocompatibility of the Sdots was evaluated using the normal prostate epithelial (PNT2) cells and the cancerous prostate (Du145) cells.[28] When both cell types were incubated with 600 μg mL^{-1} Sdots for 48 hours, cell viability was observed to be 92% for PNT2 cells and 72% for Du145 cells (Fig. 13). Thus, the compatibility of Sdots with both cell lines was confirmed through the cell viability assay, which is essential for applications such as cell labelling and imaging. The slight increase in viability for PNT2 cells was attributed to normal cell growth, as no cell death was observed.

Furthermore, confocal microscopy was employed for bioimaging to determine whether the low cytotoxicity was due to limited cellular uptake. It was observed *via* confocal imaging that the Sdots were highly permeable to the cells and were visible in both the nucleus and cytoplasm of Du145 cells after 24 hours (Fig. 14).

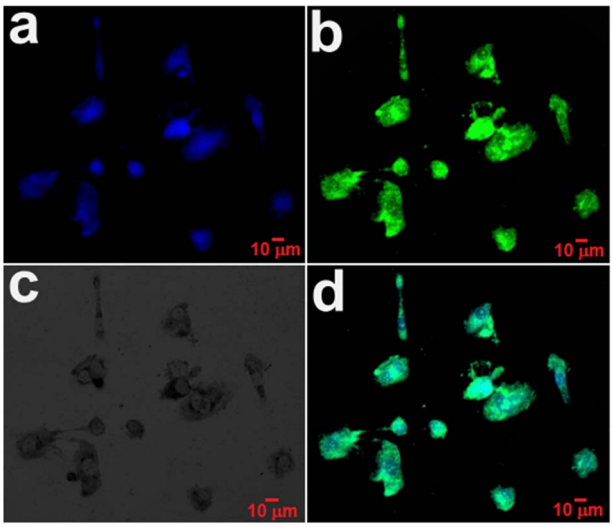

Fig. 14 Confocal microscopic images of Du-145 cells: (a) DAPI, (b) treated with Sdots, (c) bright field image, and (d) merged. Here, for 24 h the cells were treated, then fixed, and mounted in para-mount solution under coverslips. Reproduced from ref. 28 with permission from American Chemical Society, copyright 2021.

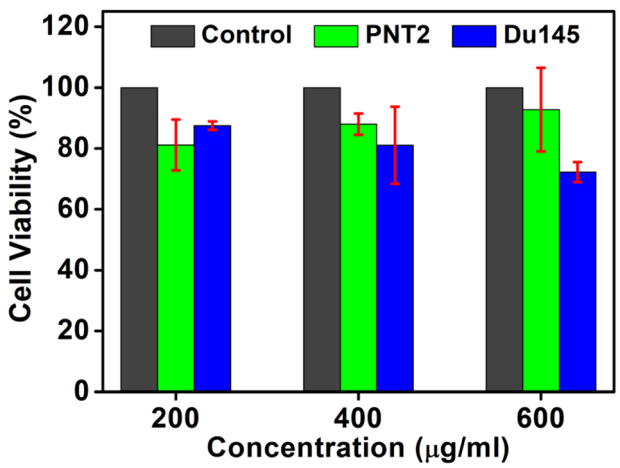

Fig. 13 Cell viability study of Sdots using the prostate epithelial (PNT2) cells and the cancerous prostate (Du145) cells. Reproduced from ref. 28 with permission from American Chemical Society, copyright 2021.

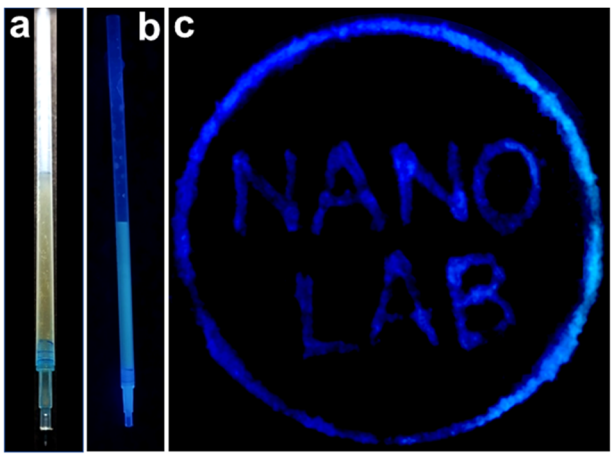

Fig. 15 Sdot-based gel ink filled in the ballpoint pen observed under (a) daylight and (b) UV light of 365 nm, (c) image of the handwriting on non-fluorescent paper under UV light. Reproduced from ref. 29 with permission from American Chemical Society, copyright 2024.

6.5 Anticounterfeiting

A UV-active gel ink was prepared using a chitosan biopolymer and the as-synthesized L-Sdots.[29] The UV-active ink was filled into a ball pen refill, and images were taken under daylight (Fig. 15a). Subsequently, images of the same refill were captured under UV light at 365 nm (Fig. 15b). Handwriting and sketches were then drawn on non-fluorescent paper using a pen filled with UV-active ink. These markings were imaged under UV light (Fig. 15c). In the image taken under daylight, no handwriting or sketches were visible. Therefore, it was concluded that the Sdot-based ink can serve as a promising tool for anticounterfeiting applications, aiding in the authentication of products and documents.

7. Challenges and future outlook

Despite the expanding interest in mechanochemical synthesis of sulfur-based nanomaterials, several challenges continue to limit its broader adoption and scientific maturity.

A key concern is scalability. While small-scale experiments, including those relying on rudimentary setups such as manual grinding with a mortar and pestle, have demonstrated promising outcomes, translating these syntheses to industrially viable scales often leads to particle agglomeration, inconsistent energy transfer, and contamination from milling media. Moreover, inert-atmosphere control, crucial for sulfur's stability and phase purity, remains difficult to maintain outside controlled lab-scale systems. Although the development of continuous or semi-batch mechanochemical systems is underway, practical implementation still requires optimisation of milling parameters, temperature regulation, and real-time monitoring.

Another persistent issue is defect regulation and reproducibility. Mechanochemistry often yields materials rich in disordered domains, sulfur vacancies, and metastable configurations. While these features can enhance properties such as photoluminescence or catalytic activity, their stochastic origin makes them difficult to control. This variability becomes particularly significant in doped systems or hybrid nanocomposites, where minor structural inconsistencies can alter performance. Integrating computational models that simulate stress propagation and reaction kinetics with *in situ* experimental tracking may provide a path toward predictive material design.

The lack of real-time mechanistic insight also remains a major hurdle. Mechanochemical sulfur transformations proceed through rapid, transient states that are difficult to isolate or observe. Although *in situ* tools such as synchrotron X-ray diffraction and time-resolved Raman spectroscopy have been explored, they remain limited in spatial and temporal resolution. Tailored *operando* platforms capable of capturing the mechanistic progression of sulfur chemistry under milling conditions are essential to elucidate bond rearrangements and intermediate formation in real-time.

Additionally, environmental and safety considerations warrant attention. The high reactivity of sulfur under mechanical stress may lead to the formation of volatile and toxic byproducts such as H_2S, especially in the presence of trace metals or residual moisture. Furthermore, extended milling cycles can generate sulfur dust and equipment wear, posing fire and health risks. Addressing these issues calls for careful reactor design, chemical compatibility of milling media, and rigorous ventilation protocols.

Looking ahead, the integration of hybrid mechanochemical strategies that combine mechanical energy with thermal, light-based, or electromagnetic inputs could enable finer control over reaction selectivity, phase evolution, and nanostructure formation. Such advancements are particularly relevant for next-generation applications in lithium–sulfur batteries, photocatalysis, and chiral sensing.

Realizing this potential will require interdisciplinary collaboration, combining expertise from mechanochemical engineering, *in situ* spectroscopy, theoretical modelling, and green chemistry. With systematic attention to these challenges, mechanochemistry could emerge as a truly transformative platform for sustainable and tunable sulfur nanomaterials.

8. Conclusion

Mechanochemistry has emerged as a versatile, sustainable, and powerful approach for synthesizing sulfur nanomaterials, offering distinct advantages over traditional solution-based or thermal methods. By employing mechanical forces to overcome activation barriers, this strategy enables the formation of defect-rich, metastable nanostructures that are otherwise inaccessible through equilibrium-based pathways. The review has outlined the mechanistic foundation of mechanochemical activation, its relevance in sulfur ring-opening and polymerization, and how this method facilitates precise tuning of structural and optical properties.

Sulfur nanomaterials obtained *via* mechanochemistry exhibit unique features, enhanced light absorption, tunable photoluminescence, strong optical stability, and, in one of the cases, CPL owing to the intricate interplay of stress-induced defects, doping, and phase transformation. These properties, in turn, drive their potential in applications such as sensing, optoelectronics, and catalysis.

While considerable progress has been made, challenges remain in understanding reaction mechanisms, controlling defect landscapes, and scaling up synthesis with reproducibility. However, with the growing integration of *in situ* techniques, computational modelling, and hybrid activation strategies, mechanochemistry is poised to redefine the design and functionalization of sulfur-based nanomaterials. This review thus presents not just a summary of current advances, but also a roadmap for future exploration in this evolving and impactful field.

Conflicts of interest

There are no conflicts to declare.

Data availability

No new data was generated or analysed as part of this review.

Acknowledgements

We thank the Department of Chemistry, AMU, Aligarh for providing research facilities.

References

1 M. Maslin, L. V. Heerde and S. Day, *Geogr. J.*, 2022, **188**, 498–505.
2 J. J. Griebel, R. S. Glass, K. Char and J. Pyun, *Prog. Polym. Sci.*, 2016, **58**, 90–125.
3 H. Mutlu, E. B. Ceper, X. Li, J. Yang, W. Dong, M. M. Ozmen and P. Theato, *Macromol. Rapid Commun.*, 2019, **40**, 1800650.
4 J. G. Wagenfeld, K. Al-Ali, S. Almheiri, A. F. Slavens and N. Calvet, *Waste Manage.*, 2019, **95**, 78–89.
5 D. A. Boyd, *Angew. Chem., Int. Ed.*, 2016, **55**, 15486–15502.
6 C. Jacob, G. I. Giles, N. M. Giles and H. Sies, *Angew. Chem., Int. Ed.*, 2003, **42**, 4742–4758.
7 F. Jalilehvand, *Chem. Soc. Rev.*, 2006, **35**, 1256–1268.
8 T. Lee, P. T. Dirlam, J. T. Njardarson, R. S. Glass and J. Pyun, *J. Am. Chem. Soc.*, 2021, **144**, 5–22.
9 S. Cherumukkil, S. Agrawal and R. V. Jasra, *ChemistrySelect*, 2023, **8**, e202204428.
10 M. K. Salman, B. Karabay, L. C. Karabay and A. Cihaner, *J. Appl. Polym. Sci.*, 2016, **133**(28), 43655.
11 Y. Teng, Q. Zhou and P. Gao, *Crit. Rev. Environ. Sci. Technol.*, 2019, **49**, 2314–2358.
12 S. L. James, C. J. Adams, C. Bolm, D. Braga, P. Collier, T. Friscic, F. Grepioni, K. D. Harris, G. Hyett, W. Jones, A. Krebs, J. Mack, L. Maini, A. G. Orpen, I. P. Parkin, W. C. Shearouse, J. W. Steed and D. C. Waddell, *Chem. Soc. Rev.*, 2012, **41**, 413–447.
13 S. Pagola, *Crystals*, 2023, **13**, 124.
14 M. Baláž, M. Achimovičová, P. Baláž, E. Dutková, M. Fabián, M. Kováčová, Z. L. Bujňáková and E. Tóthová, *Curr. Opin. Green Sustainable Chem.*, 2020, **24**, 7–13.
15 D. Ozer, in *Advances in Green Synthesis*, ed. Inamuddin, R. Boddula, M. I. Ahamed and A. Khan, Springer, Cham, 2021, vol. 2, pp. 23–39.
16 S. Kumari, S. Raturi, S. Kulshrestha, K. Chauhan, S. Dhingra, K. András, K. Thu, R. Khargotra and T. Singh, *J. Mater. Res. Technol.*, 2023, **27**, 1739–1763.
17 A. A. Belew and M. A. Assege, *Results Chem.*, 2025, **16**, 102438.
18 M. T. Swihart, *Curr. Opin. Colloid Interface Sci.*, 2003, **8**, 127–133.
19 C. Xu, S. De, A. M. Balu, M. Ojeda and R. Luque, *Chem. Commun.*, 2015, **51**, 6698–6713.
20 P. Yan, W. Zhao, F. McBride, D. Cai, J. Dale, V. Hanna and T. Hasell, *Nat. Commun.*, 2022, **13**, 4824.
21 R. Tedjini, R. Viveiros, T. Casimiro and V. D. Bonifácio, *RSC Mechanochem.*, 2024, **1**, 176–180.
22 F. K. Urakaev, A. I. Bulavchenko, B. M. Uralbekov, I. A. Massalimov, B. B. Tatykayev, A. K. Bolatov, D. N. Dzharlykasimova and M. M. Burkitbayev, *Colloid J.*, 2016, **78**, 210–219.
23 R. A. Islamov, I. Bishimova, A. N. Sabitov, A. I. Ilin and M. M. Burkitbaev, *Cell Tissue Biol.*, 2018, **12**, 27–32.
24 Z. Ma, L. Tao, D. Liu, Z. Li, Y. Zhang, Z. Liu, H. Liu, R. Chen, J. Huo and S. Wang, *J. Mater. Chem. A*, 2017, **5**, 9412–9417.
25 S. Qi, J. Sun, J. Ma, Y. Sun, K. Goossens, H. Li, P. Jia, X. Fan, C. W. Bielawski and J. Geng, *Nanotechnology*, 2019, **30**, 024001.
26 S. Turganbay, S. B. Aidarova, G. Turganbay, Y. Tileuberdi and S. L. Chen, *Int. J. Biol. Chem.*, 2019, **12**, 146–152.
27 S. Turganbay, S. Aidarova, S. Kumargaliyeva, D. Argimbayev, A. Sabitov, Z. Iskakbayeva, M. Lyu, N. Ibragimova and G. Turganbay, *ES Mater. Manuf.*, 2024, **23**, 1–11.
28 F. Arshad, M. P. Sk, S. K. Maurya and H. R. Siddique, *ACS Appl. Nano Mater.*, 2021, **4**, 3339–3344.
29 H. Hasan, N. Kulbir, P. Kumar and M. P. Sk, *J. Phys. Chem. C*, 2024, **128**, 8114–8122.
30 P. Anastas and N. Eghbali, *Chem. Soc. Rev.*, 2010, **39**, 301–312.
31 A. K. Galwey and M. E. Brown, *Thermochim. Acta*, 2002, **386**, 91–98.
32 R. A. Luirink, M. C. A. Verkade-Vreeker, J. N. M. Commandeur and D. P. Geerke, *Chembiochem*, 2020, **21**, 1461–1472.
33 A. M. Kalinkin, E. V. Kalinkina, A. A. Politov, V. N. Makarov and V. V. Boldyrev, *J. Mater. Sci.*, 2004, **39**, 5393–5398.
34 C. Xu, S. De, A. M. Balu, M. Ojeda and R. Luque, *Chem. Commun.*, 2015, **51**, 6698–6713.
35 I. J. Lin and S. Nadiv, *Mater. Sci. Eng.*, 1979, **39**, 193–209.
36 W. Ostwald, Die Chemische Literatur und die Organisation der Wissenschaft, in *Handbuch der allgemeinen Chemie*, ed. W. Ostwald and C. Drucker, Akademische Verlagsgesellschaft m. b. H., Leipzig, 1919, pp. 70–77.
37 M. C. Lea, *Br. J. Photogr.*, 1866, **13**, 84.
38 D. Braga, L. Maini and F. Grepioni, *Chem. Soc. Rev.*, 2013, **42**, 7638–7648.
39 J. F. Reynes, F. Leon and F. García, *ACS Org. Inorg. Au*, 2024, **4**, 432–470.
40 T. Friščić, C. Mottillo and H. M. Titi, *Angew. Chem.*, 2020, **132**, 1030–1041.
41 D. E. Crawford and J. Casaban, *Adv. Mater.*, 2016, **28**, 5747–5754.
42 J. F. Reynes, V. Isoni and F. García, *Angew. Chem., Int. Ed.*, 2023, **44**, e202300819.
43 M. J. Sani and A. H. Pakiari, *Comput. Theor. Chem.*, 2018, **1136–1137**, 18–28.
44 M. P. Kroonblawd and N. Goldman, *Phys. Rev. B*, 2018, **97**, 184106.
45 B. G. Kim, X. Ma, C. Chen, Y. Ie, E. W. Coir, H. Hashemi, Y. Aso, P. F. Green, J. Kieffer and J. Kim, *Adv. Funct. Mater.*, 2013, **23**, 439–445.
46 M. M. Kuklja and S. N. Rashkeev, *Phys. Rev. B: Condens. Matter Mater. Phys.*, 2007, **75**, 104111.
47 A. A. L. Michalchuk, *Faraday Discuss.*, 2023, **241**, 230–249.

48 T. Rudeichuk, D. Olekšáková, R. Maciaszek, W. Matysiak and P. Kollár, *Materials*, 2024, **17**, 862.
49 H. Petersen, S. Reichle, S. Leiting, P. Losch, W. Kersten, T. Rathmann, J. Tseng, M. Etter, W. Schmidt and C. Weidenthaler, *Chem.–Eur. J.*, 2021, **27**, 12558–12565.
50 C. Weidenthaler, *Crystals*, 2022, **12**(3), 345.
51 M. V. Chaikina, N. V. Bulina, O. B. Vinokurova, I. Y. Prosanov and D. V. Dudina, *Ceram. Int.*, 2019, **45**, 16927–16933.
52 O. M. C Chrysochoos, G. Martin, H. Caumon and J. C. Chezeaux, *Nucl. Eng. Des.*, 1989, **114**, 323–333.
53 Y. Liu, P. Liu, H. X. Lei, Y. Y. Qu, Y. Tan and F. Chen, *Appl. Surf. Sci.*, 2022, **599**(1), 153940.
54 B. K. Zhang, R. Tan, L. Y. Yang, J. X. Zheng, K. C. Zhang, S. J. Mo, Z. Lin and F. Pan, *Energy Storage Mater.*, 2018, **10**, 139–159.
55 M. D. Nothling, J. E. Daniels, Y. Vo, I. Johan and M. H. Stenzel, *Angew. Chem.*, 2023, **135**, e202218955.
56 T. R. Huff, H. Labidi, M. Rashidi, M. Koleini, R. Achal, M. H. Salomons and R. A. Wolkow, *ACS Nano*, 2017, **11**, 8636–8642.
57 N. Deneke, M. L. Rencheck and C. S. Davis, *Soft Matter*, 2020, **16**, 6230–6252.
58 A. A. L. Michalchuk and F. Emmerling, Time-resolved in situ monitoring of mechanochemical reactions, *Angew. Chem., Int. Ed.*, 2022, **61**(21), e202117270.
59 S. Lukin, K. Užarević and I. Halasz, Raman spectroscopy for real-time and in situ monitoring of mechanochemical milling reactions, *Nat. Protoc.*, 2021, **16**(7), 3492–3521.
60 B. L. d. Souza, Porous materials for lithium-sulfur batteries-mechanochemical synthesis and performance probed by in situ and operando techniques, PhD thesis, Universidade de São Paulo, 2024.
61 V. V. Boldyrev and K. Tkáčová, *J. Mater. Synth. Process.*, 2000, **8**, 121–132.
62 Z. Hao, Y. Chen, L. Wang, Y. Lu, C. He, M. Wang and X. Cui, *Diam. Relat. Mater.*, 2024, **145**, 111216.
63 Y. Li, X. Xu, B. Qiang, Y. Li, Y. Lu and C. Li, *ACS Sustainable Chem. Eng.*, 2022, **10**, 9216–9224.
64 Y. Li, X. Wang, S. Xu, B. Qiang, W. Shi, J. Gu, M. Yu and C. Li, *Sep. Purif. Technol.*, 2024, **355**, 128596.
65 T. Lee, S. Chae, J. H. Lee and S. G. Lee, *ACS Appl. Energy Mater.*, 2022, **5**, 13336–13345.
66 M. Yuasa, M. Tanaka, M. Shimizu and M. Yoshida, *J. Electrochem. Soc.*, 2022, **169**, 064515.
67 S. X. Li, D. J. Chen, F. Y. Zheng, H. F. Zhou, S. X. Jiang and Y. J. Wu, *Adv. Funct. Mater.*, 2014, **24**, 7133–7138.
68 L. H. Shen, H. N. Wang, S. N. Liu, Z. W. Bai, S. C. Zhang, X. R. Zhang and C. X. Zhang, *J. Am. Chem. Soc.*, 2018, **140**, 7878–7884.
69 L. Xiao, Q. C. Du, Y. Huang, L. Wang, S. J. Cheng, Z. Wang, T. N. Wong, E. K. L. Yeow and H. D. Sun, *ACS Appl. Nano Mater.*, 2019, **2**, 6622–6628.
70 C. X. Wang, Z. T. Wei, C. W. Pan, Z. W. Pan, X. M. Wang, J. Liu, H. Z. Wang, G. Y. Huang, M. Wang and L. Q. Mao, *Sens. Actuators, B*, 2021, **344**, 130326.
71 F. Arshad and M. P. Sk, *ACS Appl. Nano Mater.*, 2020, **3**, 3044–3049.
72 Y. H. Song, J. S. Tan, G. Wang, P. X. Gao, J. H. Lei and L. Zhou, *Chem. Sci.*, 2019, **11**, 772–777.
73 Z. Hu, H. Q. Dai, X. Wei, D. L. Su, C. Wei, Y. Y. Chen, F. X. Xie, W. L. Zhang, R. Q. Guo and S. N. Qu, *RSC Adv.*, 2020, **10**, 17266–17269.
74 A. Molla, H. Choi, H. Sakong and J. H. Youk, *Mater. Res. Bull.*, 2022, **145**, 111519.
75 H. Jin, Y. Sun, Z. Sun, M. Yang and R. Gui, *Coord. Chem. Rev.*, 2021, **438**, 213913.
76 Y. Sun, Y. Jiang, Y. Li, Q. Wang, G. Zhu, T. Yi, Q. Wang, Y. Wang, O. P. Dhankher, Z. Tan and I. Lynch, *Chem. Sci.*, 2024, **15**, 4709–4722.
77 L. Libenson, F. P. Hadley, A. P. McIlroy, V. M. Wetzel and R. R. Mellon, *J. Infect. Dis.*, 1953, **93**, 28–35.
78 S. E. A. McCallan, *Bot. Rev.*, 1949, **15**, 629–643.
79 M. Leonardi, M. Villacampa and J. C. Menéndez, *Chem. Sci.*, 2018, **9**, 2042–2064.